AGU
ADVANCING EARTH AND SPACE SCIENCE

Geophysical Research Letters

Key Points:
- A numerical model of electron flux variation to chorus elements is presented
- Bouncing electron packets are reproduced
- Electron microburst duration is estimated by the arrival time-energy dispersion analysis

Correspondence to:
L. Chen,
lunjin.chen@gmail.com

Modeling of Bouncing Electron Microbursts Induced by Ducted Chorus Waves

**Lunjin Chen[1]** iD, **Aaron W. Breneman[2]** iD, **Zhiyang Xia[1]** iD, and **Xiao-jia Zhang[3]** iD

[1]Department of Physics, University of Texas at Dallas, Richardson, TX, USA, [2]School of Physics and Astronomy, University of Minnesota, Twin Cities, Minneapolis, MN, USA, [3]Institute of Geophysics and Planetary Physics, University of California, Los Angeles, CA, USA

Abstract Short-lived (<1 s) but intense electron precipitation, known as "microbursts," may contribute significantly to electron losses in the outer radiation belt. Their origin has been suggested to correlate with resonant scattering by whistler-mode chorus waves, but existing models cannot fully explain the properties of microbursts, in particular, the bouncing electron packets in the form of a microburst that have been recently observed. A numerical model is presented that reproduces a series of electron bounce packets in response to individual chorus elements. Results indicate that the actual precipitation only occurs in the leading electron packet whereas subsequent packets form because of the following bounce motions of remaining fluxes. An analysis based on wave propagation and resonance condition yields an approximate time-energy regime of electron microbursts. Such a model is valuable for interpreting and modeling low Earth-orbiting satellite observations of electron flux variation in response to the interaction with magnetospheric chorus waves.

1. Introduction

Microbursts are impulsive (few tenths of a second) precipitation of energetic electrons (∼30 keV to >1 MeV) from the magnetosphere into the atmosphere. They have been measured through X-ray counts on balloons (e.g., Anderson & Milton, 1964; Millan, 2011; Parks et al., 1979), particle detectors on board rockets (e.g., Lampton, 1967), and low-orbiting satellites (e.g., Douma et al., 2017; Imhof et al., 1992). Although past studies suggest that microburst flux into the upper atmosphere may play an important role in radiation belt electron losses (Breneman et al., 2017; Lorentzen et al., 2001; Millan & Thorne, 2007; O'Brien et al., 2004), their importance toward the overall outer belt dynamics over this wide range of energies has yet to be fully established.

Whistler-mode chorus waves in the Earth's magnetosphere are, most likely, the primary drivers of relativistic microbursts, creating them by resonant scattering into the loss cone. This association comes from numerous observational and theoretical studies that focus on spatial (L, MLT) (Lam et al., 2010; Oliven & Gurnett, 1968) and temporal similarities (e.g., Kersten et al., 2011; Lorentzen et al., 2001), as well as plausibility of scattering mechanism (to name a few, Chang & Inan, 1983; Rosenberg et al., 1990; Saito et al., 2012). Statistically, whistler-mode chorus waves are a potential driver of relativistic microbursts (Douma et al., 2017), and the majority of microbursts are shown to have sizes consistent with the sizes of chorus waves (Shumko et al., 2020). Previous simulation with self-consistent chorus waves (Hikishima et al., 2010) has demonstrated a one-to-one correspondence between microbursts of precipitating electrons and chorus elements, which attributes the formation of an individual microburst to an interaction with one chorus element. The first observations of microburst counterpart near the equatorial plane within the outer radiation belt itself were reported (Shumko, Turner, et al., 2018). Direct testing of the process(es) of microburst creation is exceedingly difficult due to the large separation over which the chorus waves and resultant microbursts are observed. The most intense chorus waves are typically confined to within 10–20° of their source near the magnetic equator, while microbursts are observed at much higher latitudes where the size of the loss cone becomes large enough for modern instrumentation to resolve. Attempts have been made to examine detailed characteristics of those individual microbursts using low Earth-orbiting (LEO) satellites and their association with chorus waves (e.g., Breneman et al., 2017; Mozer et al., 2018). Blake and O'Brien (2016) discovered that microbursts might not just be temporal bursts of precipitation but may be very narrow, drifting "curtains" of precipitation that only appear short-lived in single-spacecraft measurements. Bouncing
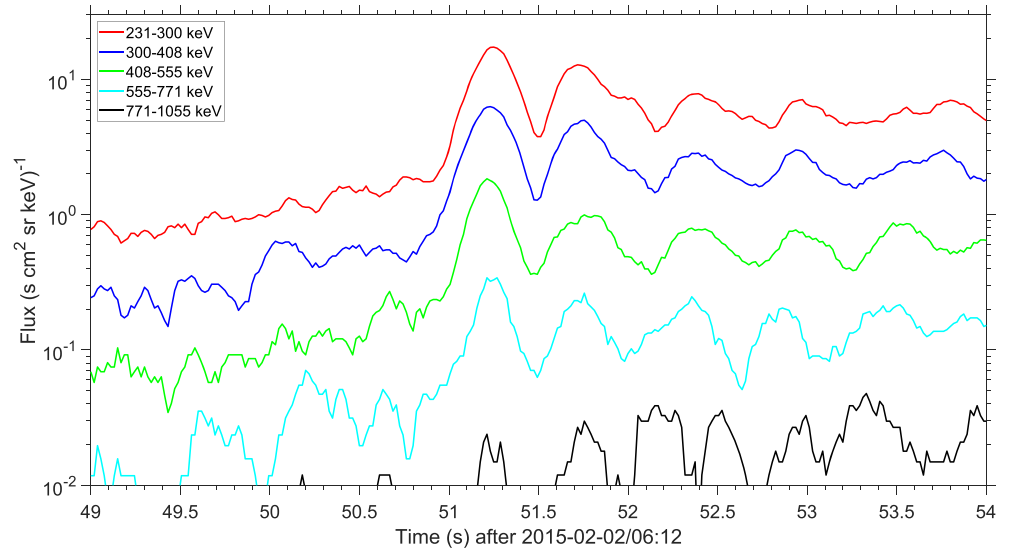
Figure 1. FIREBIRD-II FU3 CubeSat observation of bouncing electron microbursts reported by Shumko, Sample, et al. (2018). The event occurs at $\lambda = 63.4°$, longitude 15.4°, and altitude 650 km.

packets in an apparent form of microbursts have been recently reported by Shumko, Sample, et al. (2018) using the low-altitude Relativistic Electron Bursts: Intensity, Range and Dynamics II CubeSats (henceforth FIREBIRD) (Crew et al., 2016), which offered rare differential energy flux observation for microbursts. Figure 1 shows the event reported. Following the initial peak of abrupt flux enhancement, a series of microburst packets with gradually decaying electron flux peaks is observed. The time separation of the packets, which decreases with increasing electron energies, is shown to be consistent with the calculated bounce periods for each of the observed energy channels. Such bouncing packets as a group suggest a mixture of precipitating and trapped fluxes in the observation of microbursts. In this letter, we present a model of variation of electron fluxes (including trapped and precipitating electrons) at a virtual LEO satellite induced by chorus elements and address the characteristics of the resulting bouncing packets, which was not addressed by previous models (Hikishima et al., 2010; Saito et al., 2012).

2. Numerical Model

The dynamics of electrons in a dipole magnetic field and prescribed chorus wave fields is modeled by the following test particle equations along a dipole field line (with a given L value):

$$\frac{dP_z}{dt} = -\frac{\mu}{\gamma}\frac{dB}{dz} + \Sigma_j \left[qe_{jz} - qv_\perp \left(b_{jx}\sin\theta_g - b_{jy}\cos\theta_g \right) \right], \tag{1}$$

$$\frac{dP_\perp}{dt} = \frac{\mu}{\gamma}\frac{P_z}{P_\perp}\frac{dB}{dz} + \Sigma_j \left[qv_z \left(b_{jx}\sin\theta_g - b_{jy}\cos\theta_g \right) + q \left(e_{jx}\cos\theta_g + e_{jy}\sin\theta_g \right) \right], \tag{2}$$

$$\frac{dz}{dt} = v_z, \tag{3}$$

$$\frac{d\theta_g}{dt} = -\Omega/\gamma + \Sigma_j \frac{q}{P_\perp} \left[\left(e_{jy}\cos\theta_g - e_{jx}\sin\theta_g \right) + v_z \left(b_{jx}\cos\theta_g + b_{jy}\sin\theta_g \right) \right], \tag{4}$$

where B is the background dipole magnetic field strength, nonrelativistic electron gyrofrequency $\Omega = \frac{qB}{m}$, magnetic moment $\mu = P_\perp^2/(2mB)$, and q, m, v, P, θ_g, and γ are electron charge, static mass, velocity, momentum, gyrophase, and Lorentz factor, respectively. z represents dipole field line arc length with $z = 0$ defined as the equator. The subscripts z and $\perp$ denote directions parallel and perpendicular to the background magnetic field, respectively, while the subscripts x and y denote the radially outward direction and azimuthal direction toward the east, respectively. The subscript j denotes the jth chorus element with wave electric field $\mathbf{e}_j$ and magnetic field $\mathbf{b}_j$ at the electron's actual location. For the case of ducted chorus waves (parallel
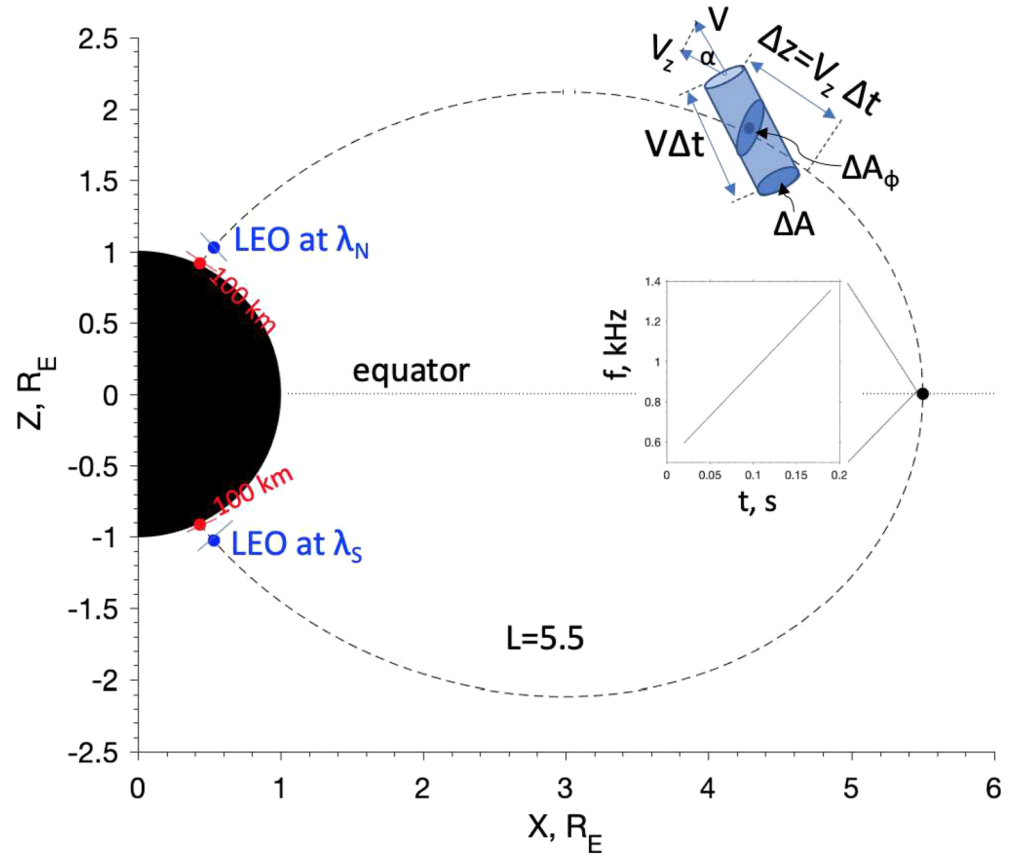
Figure 2. Illustration of simulation setup and a schematic electron flux tube. Equatorial chorus element time-frequency profile is given by the inset. An altitude of 100 km is set to the loss boundaries of test particle simulation. Virtual low Earth-orbiting satellites are located at λ_N and λ_S.

or antiparallel propagation), the wave electric ($\mathbf{e}_j$) and magnetic ($\mathbf{b}_j$) fields can be represented as $\Re\left(\tilde{\mathbf{e}}_j e^{i\phi_j}\right)$ and $\Re\left(\tilde{\mathbf{b}}_j e^{i\phi_j}\right)$, respectively, where $\Re$ denotes the real part, $\phi_j(z, t)$ is the wave phase at the guiding center along the field line, and $\tilde{\mathbf{e}}_j$ and $\tilde{\mathbf{b}}_j$ are complex amplitudes. The finite Larmor radius effect is ignored because of ducted propagation. For the equations above, gyrophase averaging on the wave force is not performed, and nonlinear wave-particle interaction is included.

Once an equatorial frequency-time profile of a chorus element is given as an input, temporal and spatial variation of wave phase $\phi_j(z, t)$ (and thus wave frequency and wave vector) can be calculated by adopting the cold plasma dispersion relation for parallel propagating whistler-mode waves (e.g., Furuya et al., 2008; Tao et al., 2012) and the modified diffusive equilibrium density model (Bortnik et al., 2011). One example of the frequency-time profile is plotted as the inset of Figure 2, where the wave frequency f rises 500 to 1,400 Hz over an interval of 0.2 s. To represent a chorus element of a flexible amplitude, the amplitude profile is implemented as $B_w(f, \lambda) = B_{w0}G(\lambda; \lambda_1, \lambda_2, \delta\lambda_1, \delta\lambda_2)G(f; f_1, f_2, \delta f_1, \delta f_2)$, where λ is magnetic latitude and B_{w0} is the maximum wave amplitude. The function G is Gaussian-like profile with a flat top and four control parameters. Specifically, $G(x; x_1, x_2, \delta x_1, \delta x_2)$ is defined as $= \exp(-(x - x_1)^2/\delta x_1^2)$ for $x < x_1$, $= \exp(-(x - x_2)^2/\delta x_2^2)$ for $x > x_2$, with values equal to unity for $x_1 \leq x \leq x_2$, where x here denotes either λ or f, and $x_1, x_2, \delta x_1$, and δx_2 are the four control parameters for the profile. To reveal the characteristics of microbursts induced by a chorus element, we set $f_1 = 600$ Hz, $f_2 = 1,350$ Hz, $\delta f_1 = 10$ Hz, $\delta f_2 = 10$ Hz, $\lambda_1 = 1°$, $\lambda_2 = 28°$, $\delta\lambda_1 = 0.1°$, $\delta\lambda_2 = 0.1°$, and $B_{w0} = 300$ pT. These latitudinal characteristics are typical for field-aligned propagating chorus waves, whereas the assumed wave amplitude corresponds to intense chorus waves in the radiation belts (e.g., Agapitov et al., 2018; Tyler et al., 2019; Zhang et al., 2018). Using the prescribed amplitude profile and the calculated wave phases, complex amplitudes of the six electromagnetic components can be obtained, and then test particle equations above can be solved. Particles that are able to reach the loss boundary, which is set to an altitude of 100 km, are considered as lost (precipitated into the upper atmosphere).

Initially, test particles are launched at $L = 5.5$ with N_g (= 120) gyrophases of equal spacing $\Delta\theta_g = 2\pi/N_g$, $N_b (= 120)$ bounce phases of equal spacing $\Delta\phi_b = 2\pi/N_b$, N_E (= 51) energies from 50 keV to 1 MeV of equal logarithmical spacing $\Delta\ln E$ and $N_{\alpha_{eq}}$ (= 45) equatorial pitch angles of equal spacing $\Delta\alpha_{eq} = 0.25°$ from $3.5°$ (just above the equatorial loss cone $\alpha_{LC} = 3.3°$ at $L = 5.5$) to $9°$. In total, 3.3×10^7 electrons are traced. For minimizing discrete nature of test particle simulation and thus modeling realistically continuously varying electron flux, each test particle represents a group of ΔN particles located inside the magnetic flux tube of interest (Figure 2) and with a range of $\Delta\theta_g$, $\Delta\phi_b$, $\Delta\alpha_{eq}$, and ΔE. Given the initial flux distribution $F_0(\alpha_{eq}, E)$, $\Delta N = F_0\Delta t\Delta A\Delta E\Delta\Omega$, where $\Delta\Omega = \sin\alpha\Delta\alpha\Delta\theta_g$ (α is the local pitch angle), $\Delta A = \Delta A_\Phi/\cos\alpha$, $\Delta t = \Delta\phi_b/\omega_b$ (ω_b is electron bounce angular frequency), and $\Delta E = E\Delta\ln E$. The cross section area of the magnetic flux tube (a constant magnetic flux $\Delta\Phi_m$) $\Delta A_\Phi = \Delta\Phi_m/B$. Virtual LEO satellites record electron fluxes in both hemispheres at $\lambda = \lambda_N$ and $\lambda = \lambda_S$ (see schematic Figure 2), corresponding to an altitude of 650 km (the altitude of the FIREBIRD observation shown in Figure 1). In this study, we adopt an anisotropic initial distribution as $F_0 = F_{0E}(E)\sin\alpha_{eq}^2$, where the energy-dependent $F_{0E}(E)$ is obtained from the Van Allen Probes flux observation at pitch angle $90°$ shown in Figure 3 of Breneman et al. (2017). Such simplified adoption of the electron anisotropy is not critical for addressing general characteristics of bouncing packets.

3. Results

The left panels of Figure 3 show the simulated electron responses over 6 s due to a single chorus element that is propagating northward, with its frequency shown as a function of latitude λ and t in Figure 3a. The chorus element starts near the equator with rising frequency and propagates to higher latitude before it completely vanishes after ~ 0.5 s. Such a short-lasting chorus wave can perturb the electron distribution by introducing nonadiabatic changes through cyclotron resonance and result in a permanent change of the electron flux distribution. Hereafter, electron flux is used to represent the averaged electron flux at virtual LEO satellites over the 4π solid angle, while precipitation (trapped) fluxes are averaged over the solid angle inside (outside) the loss cone. A series of enhanced electron fluxes is alternatively seen at λ_N (Figure 3b) and at λ_S (Figure 3c). Shortly after the appearance of the chorus element, the first enhancement of electron flux occurs in the Southern Hemisphere over the time interval of 0.5–1 s (Figure 3c) before the flux enhancements are seen in the Northern Hemisphere (Figure 3b). A few interesting points should be noted. First, the first enhancement in the Southern Hemisphere is much larger than the subsequent enhancements, because part of those electrons associated with the leading enhancement are precipitated to the lost cone boundary in the Southern Hemisphere and cannot be seen afterward by the virtual satellites. Figure 3d shows the ratio of the precipitation to trapped fluxes at λ_S. The first enhancement at λ_S contains both precipitating and trapped electrons, with the greater precipitation-to-trapped flux ratio at lower energy (attributed to the wave-particle resonance interaction near the equator). In subsequent bounce cycles, only the trapped electrons can be seen later at λ_N and λ_S, meaning no actual precipitation occurs at the Northern Hemisphere. Second, the successive flux enhancements are separated by a fraction of a second, depending on the electron energy. This is caused by the bounce motion of the trapped electrons, with a shorter bounce period for higher energy. Such periodic flux enhancements can be maintained for the entire simulation time interval (6 s) because the bounce period weakly depends on α_{eq}. Third, it takes some time for those electrons affected by the interaction with the chorus element in the Northern Hemisphere to arrive at the virtual location λ_S in the Southern Hemisphere and then to arrive at the virtual location λ_N in the Northern Hemisphere. To resonate with the northward propagating chorus wave, electrons must be countermoving to the south in order to satisfy the Doppler-shifted resonance condition. Fourth, although short lived, the chorus element can produce the permanent change to electron distribution, not only in the form of precipitation but also through those bouncing packets of trapped electrons. Fifth, modeled fluxes are almost constant except when electrons affected by the chorus fields arrive, verifying that the algorithm of modeling fluxes works properly. Sixth, due to the integral energy bin used in flux measurement (e.g., FIREBIRD-II), the fluxes averaged over the energy bin width will appear to spread faster than those in Figures 3b and 3c, because energy dependence of bounce period leads to mixing of bounce phases. For example, the averaged fluxes over 80–150 and 150–300 keV are shown in Figure 3e. One can see that the electron fluxes averaged over an energy range will appear as an abrupt enhancement followed by bouncing packets with apparently decaying peaks and spread duration, roughly separated by the bounce period.
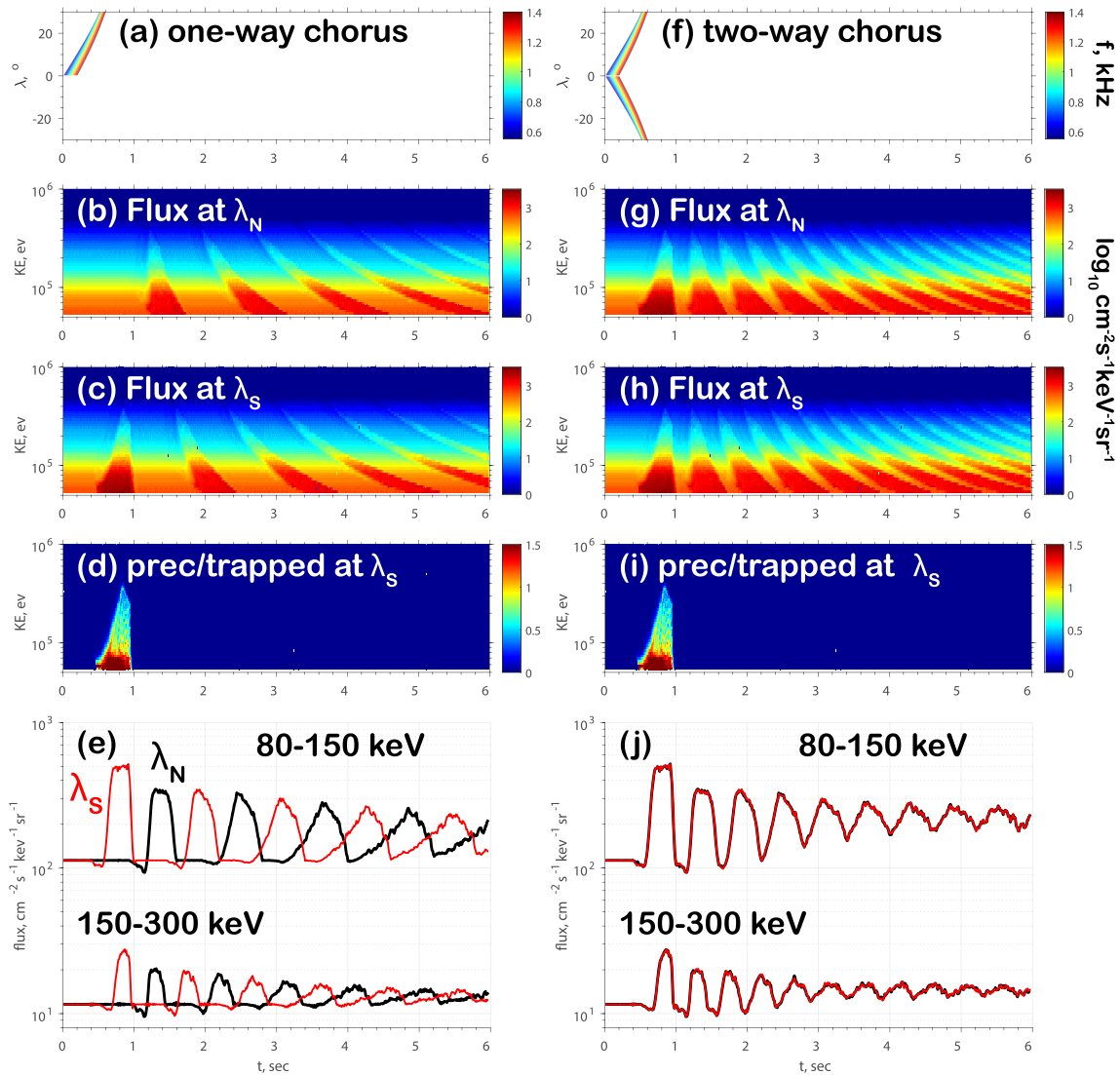
Figure 3. Simulation of electron responses to a northward propagating chorus element (left) and to two oppositely propagating chorus elements (right). Chorus frequency as a function of time and latitude (a, f). Electron fluxes (b, g) at λ_N and (c, h) at λ_S. The ratio of precipitation flux to trapped flux (d, i) at $\lambda = \lambda_S$. Electron fluxes averaged over the selected energy channel, 80–150 and 150–300 keV, are shown in panels (e) and (j) with the black lines for $\lambda = \lambda_N$ and the red lines for $\lambda = \lambda_S$.

We also perform another simulation run with a pair of oppositely propagating chorus elements (Figure 3f) by adding another similar chorus element but with southward propagation. Here, we highlight some comparison with the simulation results for a single northward propagating chorus element. For the two-way chorus elements, electron fluxes at λ_N and λ_S are identical (Figures 3g and 3h) due to two simultaneous series of bouncing packets. The two series of bouncing packets form at a fixed latitude so that the electron flux appears as an abrupt enhancement followed by trailing packets every half electron bounce period instead of the whole electron bounce period. The ratio of precipitating to trapped electron flux at λ_S (Figure 3i) is the same as that for a single element (Figure 3d), but the actual precipitation due to the two-way chorus takes place in both hemispheres. For the virtual flux measurement over an energy bin (Figure 3j), the fluxes are the same at λ_N and λ_S and are subject to decay every half electron bounce (Figure 3j). As a result, two simultaneous bouncing packets might overlap at a fixed location as they are spread in time duration.

To examine microburst duration characteristics, we analyze the arrival time-energy dispersion of the first enhanced electron flux shown in Figure 3c. We rerun the first simulation case over a shorter interval (1.5 s) but increase the number of test particle energies by extending down to 10 keV. The simulated electron flux is shown in Figure 4a. Although the flux intensity depends on the initial flux distribution and the efficiency
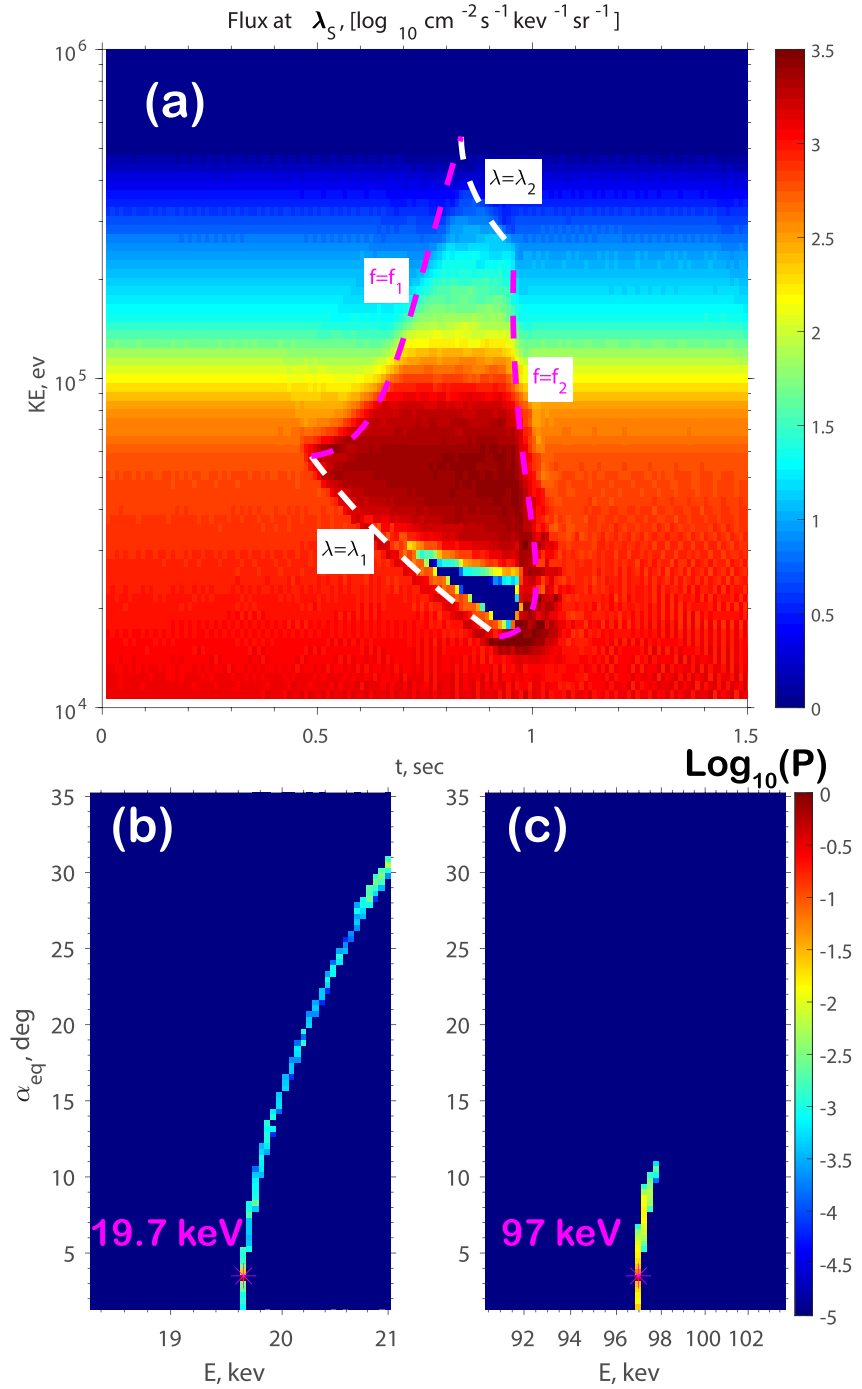
Figure 4. (a) Zoom-in plot of electron flux response at $\lambda = \lambda_S$ in Figure 3c. Four energy-time dispersion curves for $\lambda = \lambda_1$, $\lambda = \lambda_2$, $f = f_1$, and $f = f_2$ are shown as dashed lines. (b) The probability of α_{eq} and E for electrons with initial energy $E_0 = 19.7$ keV and $\alpha_{eq,0} = 3.5°$ after the interaction with the chorus element. (c) Similar to (b) but for initial energy $E_0 = 97$ keV.

of wave-particle interaction, the shape of the electron flux response can be estimated based on the energy dispersion of the electron arrival time.

Let us consider resonant electrons at the loss cone edge (α_{LC}) moving to the south, a chorus element traveling north, and a virtual observation location in the Southern Hemisphere (z_S). The arrival time can be obtained

by solving the gyroresonance condition at a given location z with a given frequency ω and kinematics of wave propagation and electron adiabatic motion, similar to the time-of-flight analysis in Saito et al. (2012).

$$t_{\text{arrival}} = t_0(\omega) + \int_0^z \frac{dz'}{v_g(\omega, z')} + \tau_b \left(\frac{1}{\tau_b} \int_z^{z_S} \frac{dz'}{v_z(z')} \right), \tag{5}$$

$$\omega - k_z(z)v_z = -\Omega(z)/\gamma, \tag{6}$$

$$\sin^2\alpha_{LC}/B(z=0) = \sin^2\alpha/B(z), \tag{7}$$

where $t_0(\omega)$ is the time when chorus angular frequency reaches ω at the equator, $\tau_b = 0.117\frac{L}{v/c}(1 - 0.4635\sin^{0.75}\alpha_{LC})$ (Walt, 1994) is the electron bounce period evaluated at the loss cone, v_g (>0) is the group velocity of chorus wave, and v_z (<0) is parallel velocity of electron adiabatic motion for $\alpha_{eq} = \alpha_{LC}$. The second and third terms on the right-hand side of Equation 5 represent, respectively, the time for the chorus wave with frequency ω to arrive at resonant location z and the time for the resonant electron to arrive the observation location z_S from the resonant location z. For chorus frequency much greater than ion gyrofrqeuency, $v_g = \frac{2c}{\omega_{pe}/|\Omega_e|}(1 - \omega/|\Omega_e|)^{3/2}(\omega/|\Omega_e|)^{1/2}$, where ω_{pe} is electron plasma frequency, and v_g maximizes as $\frac{3\sqrt{3}c}{8\omega_{pe}/|\Omega_e|}$ at $\omega/|\Omega_e|=1/4$. The factor inside the parentheses of the third term is independent of electron energy E. From Equations 6 and 7, the resonant energy E_{res} can be obtained as a function of ω and z, and E_{res} increases with decreasing ω and increasing z. Then from Equation 5, t_{arrival} can be obtained as a function of ω and z too. Given the two frequency boundaries (f_1 and f_2) and the two latitudinal boundaries (λ_1 and λ_2) of the chorus wave amplitude profile, four energy-time dispersion curves, corresponding to each of the four boundaries, are plotted in Figure 4a. One can see the four curves enclose well the affected electron flux at the virtual location λ_S (corresponding to z_S). For a fixed λ (the two black dashed lines in Figure 4a), as ω increases, E decreases, and $t_{arrival}$ also increases because $t_0(\omega)$ increases and τ_b increases (due to decreasing E), although the wave propagation time decreases slightly for $\omega < |\Omega_e|/4$. For a fixed ω (the two magenta dashed lines in Figure 4a), as z (or λ) increases, E increases while $t_{arrival}$ may increases or decreases. At the lower frequency boundary $f = f_1$, $t_{arrival}$ increases, while at the upper frequency boundary $f = f_2$, $t_{arrival}$ increases and then decreases. This is because, as λ increases (and thus E increases), the wave propagation time increases and the factor in the parentheses of Equation 5 increases while τ_b decreases. The longer wave propagation time and longer latitudinal transit range for higher E explains why electrons at 80–150 keV arrive earlier than those at 150–300 keV. Finally, two additional comments are worthy mentioning: (1) Even with nonlinear wave-particle interactions taken into account, the simplified arrival time-energy dispersion analysis mentioned above works well since they occur in the vicinity of the gyroresonance condition (Equation 6); (2) Microburst energy shown in Figure 3 has a upper cutoff near ~400 keV, but even higher energy (e.g., MeV) microbursts can occur for lower plasma density, which increases electron minimum resonant energy.

From this arrival time-energy dispersion analysis, one can see the duration of electron microbursts can be estimated and is controlled either by the lower frequency boundary and the upper-latitude boundary of the chorus wave element or by the lower and upper frequency boundaries, the latter of which has been recognized in the analysis of Saito et al. (2012). One might expect a shorter duration for electron microbursts at fixed energy (especially higher energy) is favored for a shorter duration and a narrower frequency range of a chorus element at the equator or a narrower latitudinal range of a chorus element. For the case considered in Figure 4a, electron microbursts can last less than 0.2 s above 200 keV and up to 0.5 s at 40 keV.

It should be worth noting that there exists electron flux depletion instead of enhancement near 20 keV, as a result of the interaction with the chorus wave near the equator. There are three known means of transport of electrons due to wave-particle interaction with chorus waves (e.g., Bortnik et al., 2008; Tao et al., 2012): random scattering, phase bunching that transports toward smaller α_{eq} (and smaller E), and phase trapping toward higher α (and higher E). The change of E and the change of α_{eq} due to resonant interaction with parallel chorus waves should have the same sign (e.g., Summers et al., 1998). The pitch angle scattering together with a positive pitch angle gradient near the loss cone leads to a net transport toward smaller α_{eq}, as is the case with phase bunching. Figure 4b shows the probability of final α_{eq} and E of 14,400 ($N_b \times N_g$) test particles with initial $\alpha_{eq0} = 3.5°$ and $E_0 = 19.7$ keV after the interaction with the chorus element. A significant increase of α_{eq} by 30° (Figure 4b) is caused by the phase trapping with the equatorial chorus element, which

is also known as anomalous phase trapping of electrons at small pitch angles (Gan et al., 2020; Kitahara & Katoh, 2019). Those electron trajectories (not shown) are similar to Figure 3 of Kitahara and Katoh (2019). Such anomalous phase trapping leads to a reduction of those electrons near the loss cone and thus a reduction of electron flux at the virtual LEO satellite. Figure 4c shows the probability for electrons with initial energy $E_0 = 97$ keV, where the other two mechanisms (random scattering and phase bunching) due to the chorus wave off the equator are dominant. As a consequence, electron fluxes at lower α_{eq} increase, and enhancement of electron flux is seen at the virtual location.

4. Conclusions and Discussion

We model electron flux response (including trapped and precipitating electrons) due to ducted chorus elements and perform the arrival-time-energy dispersion analysis to characterize microburst duration as a function of energy. The bouncing electron packets for a microburst event observed on FIREBIRD are reproduced for both one-way and two-way propagating chorus waves, and the comparison is made between the two cases. Our principal conclusions are summarized as follows:

- A numerical model of electron flux variation to chorus elements is presented. Such a model is valuable when interpreting the cause of microburst flux and predicting electron flux variation at a virtual observation.
- Bouncing electron packets are reproduced. A single chorus element will produce bouncing packets with a bounce period spacing, while counterpropagating chorus elements will produce bouncing packets with a half bounce period. For the leading packet, the precipitation-to-trapped electron flux ratio tends to be greater at lower energies.
- Energy-dependent electron microburst duration (approximately a fraction of a second) can be estimated by the arrival time-energy dispersion analysis. A shorter microburst duration is favored for shorter-duration chorus packets and for chorus packets with a narrower frequency range and a narrower latitudinal range.
- Our modeling results show that a reduction of electron flux at relatively low energies (tens of keV) at virtual LEO satellite locations can occur as a result of phase trapping induced by the chorus waves near the equator.

Bouncing electron packets of decaying flux peaks (Figure 1) in the Northern Hemisphere are roughly separated by the bounce period in the event reported by Shumko, Sample, et al. (2018). They may be interpreted as the interaction of a single southward propagating chorus, in the absence of the northward counterpart. Such a hemispheric asymmetry of chorus waves may exist if there exists an ultralow-frequency wave which can cause an asymmetric perturbation of the background plasma or energetic electron distribution. Another possible source of the asymmetry is the nondipolar magnetic field especially for large L shell. For hemispherically symmetric chorus waves, the bouncing packets, if present, should be separated by half an electron bounce period instead of one whole electron bounce period. Electron bouncing packets could form for a single chorus element or two-way chorus elements or for a series of chorus elements with time separation exceeding the electron bounce period.

Our study is limited to the case of ducted (parallel or antiparallel) propagation, which usually requires fine-scale density structures. Unducted propagation in a smooth density distribution could lead to the obliqueness of chorus elements (e.g., Lu et al., 2019). In addition, unducted chorus waves will spread their energy over a range of magnetic field lines and thus have a shorter duration on a given field line which could shorten the microburst duration and therefore reduce the energy dispersion of electron precipitation. The extension of modeling electron responses due to the unducted chorus is left as a future investigation.

As a final remark, this study focuses on electron responses to individual chorus waves and retains the dynamics on the timescale of electron bounce periods. Long-term evolution due to nonlinear wave-particle interaction with a group of chorus waves can be modeled by a modified Fokker-Planck equation with the inclusion of phase trapping as probabilistic but fast transport (Artemyev et al., 2017, 2018). A different description based on the Markov chain is adopted by Zheng et al. (2019) to model nonlinear wave-particle interaction between electrons and electromagnetic ion cyclotron waves and is also capable of modeling the chorus wave interaction.

Data Availability Statement

The FIREBIRD-II data are available online (at https://solar.physics.montana.edu/FIREBIRD_II/). The simulation results shown in the paper are available online (at https://zenodo.org/record/3973650#.XysdnBNKjHd).

References

Agapitov, O. V., Mourenas, D., Artemyev, A. V., Mozer, F. S., Hospodarsky, G., Bonnell, J., & Krasnoselskikh, V. (2018). Synthetic empirical chorus wave model from combined Van Allen Probes and cluster statistics. *Journal of Geophysical Research: Space Physics*, *123*, 297–314. https://doi.org/10.1002/2017JA024843

Anderson, K. A., & Milton, D. W. (1964). Balloon observations of X rays in the auroral zone: 3. High time resolution studies. *Journal of Geophysical Research*, *69*(21), 4457–4479. https://doi.org/10.1029/JZ069i021p04457

Artemyev, A. V., Neishtadt, A. I., Vasiliev, A. A., & Mourenas, D. (2017). Probabilistic approach to nonlinear wave-particle resonant interaction. *Physical Review E*, *95*(23), 204. https://doi.org/10.1103/PhysRevE.95.023204

Artemyev, A. V., Neishtadt, A. I., Vasiliev, A. A., & Mourenas, D. (2018). Long-term evolution of electron distribution function due to nonlinear resonant interaction with whistler mode waves. *Journal of Plasma Physics*, *84*(2), 905840206. https://doi.org/10.1017/S0022377818000260

Blake, J. B., & O'Brien, T. P. (2016). Observations of small-scale latitudinal structure in energetic electron precipitation. *Journal of Geophysical Research: Space Physics*, *121*, 3031–3035. https://doi.org/10.1002/2015JA021815

Bortnik, J., Chen, L., Li, W., Thorne, R. M., & Horne, R. B. (2011). Modeling the evolution of chorus waves into plasmaspheric hiss. *Journal of Geophysical Research*, *116*, A08221. https://doi.org/10.1029/2011JA016499

Bortnik, J., Thorne, R. M., & Inan, U. S. (2008). Nonlinear interaction of energetic electrons with large amplitude chorus. *Geophysical Research Letters*, *35*, L21102. https://doi.org/10.1029/2008GL035500

Breneman, A. W., Crew, A., Sample, J., Klumpar, D., Johnson, A., Agapitov, O., et al. (2017). Observations directly linking relativistic electron microbursts to whistler mode chorus: Van Allen Probes and FIREBIRD II. *Geophysical Research Letters*, *44*, 11,265–11,272. https://doi.org/10.1002/2017GL075001

Chang, H. C., & Inan, U. S. (1983). A theoretical model study of observed correlations between whistler mode waves and energetic electron precipitation events in the magnetosphere. *Journal of Geophysical Research*, *88*(A12), 10,053–10,064. https://doi.org/10.1029/JA088iA12p10053

Crew, A. B., Spence, H. E., Blake, J. B., Klumpar, D. M., Larsen, B. A., O'Brien, T. P., et al. (2016). First multipoint in situ observations of electron microbursts: Initial results from the NSF FIREBIRD II mission. *Journal of Geophysical Research: Space Physics*, *121*, 5272–5283. https://doi.org/10.1002/2016JA022485

Douma, E., Rodger, C. J., Blum, L. W., & Clilverd, M. A. (2017). Occurrence characteristics of relativistic electron microbursts from SAMPEX observations. *Journal of Geophysical Research: Space Physics*, *122*, 8096–8107. https://doi.org/10.1002/2017JA024067

Furuya, N., Omura, Y., & Summers, D. (2008). Relativistic turning acceleration of radiation belt electrons by whistler mode chorus. *Journal of Geophysical Research*, *113*, A04224. https://doi.org/10.1029/2007JA012478

Gan, L., Li, W., Ma, Q., Albert, J. M., Artemyev, A. V., & Bortnik, J. (2020). Nonlinear interactions between radiation belt electrons and chorus waves: Dependence on wave amplitude modulation. *Geophysical Research Letters*, *47*, e2019GL085987. https://doi.org/10.1029/2019GL085987

Hikishima, M., Omura, Y., & Summers, D. (2010). Microburst precipitation of energetic electrons associated with chorus wave generation. *Geophysical Research Letters*, *37*, L07103. https://doi.org/10.1029/2010GL042678

Imhof, W. L., Voss, H. D., Mobilia, J., Datlowe, D. W., Gaines, E. E., McGlennon, J. P., & Inan, U. S. (1992). Relativistic electron microbursts. *Journal of Geophysical Research*, *97*(A9), 13,829–13,837. https://doi.org/10.1029/92JA01138

Kersten, K., Cattell, C. A., Breneman, A., Goetz, K., Kellogg, P. J., Wygant, J. R., et al. (2011). Observation of relativistic electron microbursts in conjunction with intense radiation belt whistler-mode waves. *Geophysical Research Letters*, *38*, L08107. https://doi.org/10.1029/2011GL046810

Kitahara, M., & Katoh, Y. (2019). Anomalous trapping of low pitch angle electrons by coherent whistler mode waves. *Journal of Geophysical Research: Space Physics*, *124*, 5568–5583. https://doi.org/10.1029/2019JA026493

Lam, M. M., Horne, R. B., Meredith, N. P., Glauert, S. A., Moffat-Griffin, T., & Green, J. C. (2010). Origin of energetic electron precipitation >30 keV into the atmosphere. *Journal of Geophysical Research*, *115*, A00F08. https://doi.org/10.1029/2009JA014619

Lampton, M. (1967). Daytime observations of energetic auroral-zone electrons. *Journal of Geophysical Research*, *72*(23), 5817–5823. https://doi.org/10.1029/JZ072i023p05817

Lorentzen, K. R., Blake, J. B., Inan, U. S., & Bortnik, J. (2001). Observations of relativistic electron microbursts in association with VLF chorus. *Journal of Geophysical Research*, *106*, 6017–6028. https://doi.org/10.1029/2000JA003018

Lu, Q., Ke, Y., Wang, X., Liu, K., Gao, X., Chen, L., & Wang, S. (2019). Two-dimensional gcPIC simulation of rising-tone chorus waves in a dipole magnetic field. *Journal of Geophysical Research: Space Physics*, *124*, 4157–4167. https://doi.org/10.1029/2019JA026586

Millan, R. (2011). Understanding relativistic electron losses with BARREL. *Journal of Atmospheric and Solar-Terrestrial Physics*, *73*(11), 1425–1434. https://doi.org/10.1016/j.jastp.2011.01.006

Millan, R., & Thorne, R. (2007). Review of radiation belt relativistic electron losses. *Journal of Atmospheric and Solar-Terrestrial Physics*, *69*(3), 362–377. https://doi.org/10.1016/j.jastp.2006.06.019

Mozer, F. S., Agapitov, O. V., Blake, J. B., & Vasko, I. Y. (2018). Simultaneous observations of lower band chorus emissions at the equator and microburst precipitating electrons in the ionosphere. *Geophysical Research Letters*, *45*, 511–516. https://doi.org/10.1002/2017GL076120

O'Brien, T. P., Looper, M. D., & Blake, J. B. (2004). Quantification of relativistic electron microburst losses during the GEM storms. *Geophysical Research Letters*, *31*, L04802. https://doi.org/10.1029/2003GL018621

Oliven, M. N., & Gurnett, D. A. (1968). Microburst phenomena: 3. An association between microbursts and VLF chorus. *Journal of Geophysical Research*, *73*(7), 2355–2362. https://doi.org/10.1029/JA073i007p02355

Parks, G. K., Gurgiolo, C., & West, R. (1979). Relativistic electron precipitation. *Geophysical Research Letters*, *6*(5), 393–396. https://doi.org/10.1029/GL006i005p00393

Rosenberg, T. J., Wei, R., Detrick, D. L., & Inan, U. S. (1990). Observations and modeling of wave-induced microburst electron precipitation. *Journal of Geophysical Research*, *95*(A5), 6467–6475. https://doi.org/10.1029/JA095iA05p06467

Saito, S., Miyoshi, Y., & Seki, K. (2012). Relativistic electron microbursts associated with whistler chorus rising tone elements: GEMSIS-RBW simulations. *Journal of Geophysical Research*, *117*, A10206. https://doi.org/10.1029/2012JA018020

Shumko, M., Johnson, A. T., Sample, J. G., Griffith, B. A., Turner, D. L., O'Brien, T. P., et al. (2020). Electron microburst size distribution derived with AeroCube-6. *Journal of Geophysical Research: Space Physics*, *125*, e2019JA027651. https://doi.org/10.1029/2019JA027651

Shumko, M., Sample, J., Johnson, A., Blake, B., Crew, A., Spence, H., et al. (2018). Microburst scale size derived from multiple bounces of a microburst simultaneously observed with the FIREBIRD-II CubeSats. *Geophysical Research Letters*, *45*, 8811–8818. https://doi.org/10.1029/2018GL078925

Shumko, M., Turner, D. L., O'Brien, T. P., Claudepierre, S. G., Sample, J., Hartley, D. P., et al. (2018). Evidence of microbursts observed near the equatorial plane in the outer Van Allen radiation belt. *Geophysical Research Letters*, *45*, 8044–8053. https://doi.org/10.1029/2018GL078451

Summers, D., Thorne, R. M., & Xiao, F. (1998). Relativistic theory of wave-particle resonant diffusion with application to electron acceleration in the magnetosphere. *Journal of Geophysical Research*, *103*(A9), 20,487–20,500. https://doi.org/10.1029/98JA01740

Tao, X., Bortnik, J., Thorne, R. M., Albert, J. M., & Li, W. (2012). Effects of amplitude modulation on nonlinear interactions between electrons and chorus waves. *Geophysical Research Letters*, *39*, L06102. https://doi.org/10.1029/2012GL051202

Tyler, E., Breneman, A., Cattell, C., Wygant, J., Thaller, S., & Malaspina, D. (2019). Statistical distribution of whistler mode waves in the radiation belts with large magnetic field amplitudes and comparison to large electric field amplitudes. *Journal of Geophysical Research: Space Physics*, *124*, 6541–6552. https://doi.org/10.1029/2019JA026913

Walt, M. (1994). *Introduction to geomagnetically trapped radiation* (Vol. 10). New York: Cambridge University Press.

Zhang, X.-J., Thorne, R., Artemyev, A., Mourenas, D., Angelopoulos, V., Bortnik, J., et al. (2018). Properties of intense field-aligned lower-band chorus waves: Implications for nonlinear wave-particle interactions. *Journal of Geophysical Research: Space Physics*, *123*, 5379–5393. https://doi.org/10.1029/2018JA025390

Zheng, L., Chen, L., & Zhu, H. (2019). Modeling energetic electron nonlinear wave-particle interactions with electromagnetic ion cyclotron waves. *Journal of Geophysical Research: Space Physics*, *124*, 3436–3453. https://doi.org/10.1029/2018JA026156